ACS Photonics

Barrier Height Tuning of Terahertz Quantum Cascade Lasers for High-Temperature Operation

Martin Alexander Kainz,*[†,‡] Sebastian Schönhuber,[†,‡] Aaron Maxwell Andrews,[∥,‡] Hermann Detz,[§,‡] Benedikt Limbacher,[†,‡] Gottfried Strasser,[∥,‡] and Karl Unterrainer[†,‡]

[†]Photonics Institut, TU Wien, 1040 Vienna, Austria
[‡]Center for Micro- and Nanostructures, TU Wien, 1040 Vienna, Austria
[∥]Institute of Solid State Electronics, TU Wien, 1040 Vienna, Austria
[§]Central European Institute of Technology, Brno University of Technology, 61200 Brno, Czech Republic

ABSTRACT: Terahertz quantum cascade lasers (QCLs) are excellent coherent light sources, but are still limited to an operating temperature below 200 K. To tackle this, we analyze the influence of the barrier height for the identical three-well terahertz QCL layer sequence by comparing different aluminum concentrations (x = 0.12−0.24) in the GaAs/Al$_x$Ga$_{1-x}$As material system, and then we present an optimized structure based on these findings. Electron injection and extraction mechanisms as well as LO-phonon depopulation processes play crucial roles in the efficient operation of these lasers and are investigated in this study. Experimental results of the barrier height study show the highest operating temperature of 186.5 K for the structure with 21% aluminum barriers, with a record $k_B T_{max}/\hbar\omega$ value of 1.36 for a three-well active region design. An optimized heterostructure with 21% aluminum concentration and reduced cavity waveguide losses is designed and enables a record operating temperature of 196 K for a 3.8 THz QCL.

KEYWORDS: quantum cascade lasers, terahertz, molecular beam epitaxy, optical phonon, quantized transitions
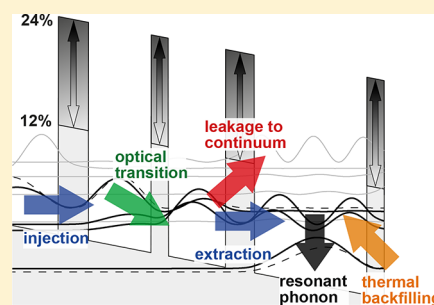
Terahertz (THz) quantum cascade lasers (QCLs) are compact semiconductor coherent light sources with high optical power in the frequency range between 1.2 and 5.4 THz.[1−4] This spectral region is of great interest for spectroscopic applications including gas sensing and astronomy THz heterodyne receivers.[5,6] A limited operating temperature range prevents these fields to take full advantage of THz QCLs. In the first years after their development, a steady increase in the maximum pulsed operating temperature (T_{max}) was achieved, reaching almost 200 K.[7] Since 2012, much effort has been devoted to increasing the T_{max}, including different active region designs as well as quantum cascade structures based on novel material systems. Designs with improved LO-phonon-assisted depopulation process via a double extraction mechanism[8] or a double-phonon resonant depopulation[9] have been realized. Heterostructures with higher barriers for reduced carrier leakage were studied.[10,11] Alternative material systems to GaAs/AlGaAs, with lower effective electron mass, are promising because the optical gain in the heterostructure scales inversely to the effective mass.[12,13] Such materials include InGaAs/InAlAs,[14,15] InGaAs/AlGaInAs,[16−18] InGaAs/GaAsSb,[19] and InAs/AlAsSb[20] with material compositions lattice matched to InP and InAs, respectively. The first three material systems suffer from very thin barriers and interface roughness effects but show already good results with maximum operation temperatures of 155 K and output powers up to 600 mW in pulsed operation.[15] InAs wells are favorable, having the lowest effective mass;

however, to date, lasing could only be achieved in an applied magnetic field.[20] Unfortunately, these different approaches did not succeed in improving the operating temperature of THz QCLs, which is mainly restricted by three main effects. At elevated temperatures the in-plane energy of electrons in the upper laser level is sufficiently increased to make LO-phonon emission possible, the so-called thermally activated LO-phonon scattering, which reduces the upper level lifetime.[2,21] Second, thermal backfilling into the lower laser level, which can be attributed to the Boltzmann distribution, decreases the population inversion at elevated temperatures.[2] The third effect is the increased leakage of electrons into continuum states at elevated temperatures.[22] Thermally activated backfilling and especially leakage into the continuum can be related to the electron confinement within the heterostructure. To address these problems, we measure the influence of different conduction band offsets (CBOs) for active regions with an identical layer sequence. The standard material system for THz QCLs GaAs/Al$_x$Ga$_{1-x}$As, which remains a direct band gap semiconductor up to 45% aluminum, allows the adjustment of the barrier height. In contrast to the study of the lower effective mass materials, where interface roughness complicates the study of different barrier heights,[18,23] the interface roughness for GaAs/AlGaAs does not change significantly for higher Al

concentrations. Thus, GaAs/AlGaAs is an ideal material for studying the influence of different CBOs on electrical and optical properties for quantum cascade structures.

In the first part of this paper, we discuss the influence of barrier heights obtained by band structure calculations and describe the effects on important properties like electrical stability, LO-phonon depopulation mechanism, oscillator strength (f_{43}), and lasing frequency. In the second part, we present the experimental results and clarify the important role of CBO engineering for improved temperature operation of THz QCLs. In the last part of this paper, we explain how these new findings can be used to improve the active region design for higher operating temperatures to achieve a record of 196 K for a 3.8 THz QCL.

HETEROSTRUCTURE DESIGN

To study the influence of the barrier height, we investigate five active regions with an identical layer sequence of the GaAs/$Al_xGa_{1-x}As$ heterostructure using the barrier compositions x = 0.12, 0.15, 0.18, 0.21, and 0.24. The quantum cascade structure is based on the three-well active region design with resonant LO-phonon depopulation. Until now, this design enabled the highest reported operating temperature for THz QCLs.[7] We use the same layer structure; however, the doping profile is shifted away from the lasing transition to counteract dopant migration effects during epitaxial growth. Previous works demonstrated the importance of dopant position engineering for THz QCLs to reduce impurity scattering effects and thus increase the maximum operating temperature.[15,24] The heterostructure design and the doping profile are shown in Figure 1. This figure also shows the variable CBO, where the depicted electron wave functions belong to the band structure with an Al concentration of 15%.
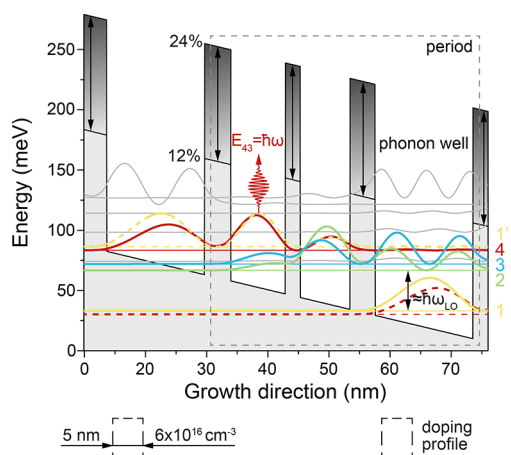
Figure 1. Band structure of the investigated three-well resonant LO-phonon quantum cascade design. The different conduction band offsets are indicated with the arrows in the barrier for aluminum concentrations from 12% to 24%. The depicted energy levels and squared wave functions belong to the structure with 15% for an applied bias field of 12.1 kV/cm. The optical transition takes place between levels |4⟩ and |3⟩, whereas the energy difference of levels |2⟩ and |1⟩ is in resonance with the LO-phonon of GaAs. The dashed gray frame indicates one single period of the structure. The doping profile is depicted at the bottom of the figure, showing the shifted doping away from the optical transition.

BAND STRUCTURE CALCULATIONS

Since we first only want to study the influence of the barrier height and not that of the design we keep the layer thicknesses unchanged and only modify the barrier height of the quantum cascade design. The different barrier compositions change the CBO from 96 to 192 meV and increase the effective electron mass in the barrier from 0.077 to 0.087 m_0. Barrier compositions lower than 12% result in unbound first excited states in the phonon well, therefore the study of such low barriers is irrelevant. For barriers containing more than 24% Al, the change in the wave functions is already too much, thus the injection and extraction mechanism does not align properly anymore. Figure 2
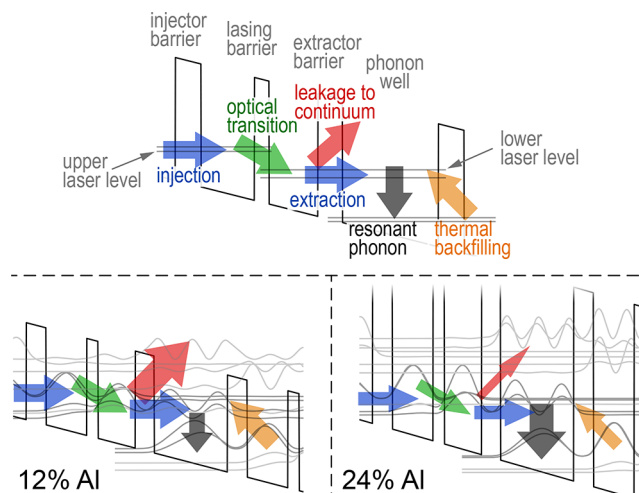
Figure 2. Schematic of the involved electron processes in the three-well active region. Two designs with 12% and 24% Al barrier composition are compared. The higher CBO results in a reduced electron injection and extraction mechanism due to lower tunneling probabilities. The larger electron mode confinement caused by the larger CBO leads to a more diagonal optical transition. Low barriers increase the electron leakage to continuum states, whereas the larger energy separation in the phonon well is beneficial for higher barriers.

depicts a simple description of electron transport processes in the investigated THz QCLs and compares the designs with 12% and 24% Al barrier composition. Thermal backfilling and electron leakage into the continuum are lower for higher barriers. The first process can be explained by the Boltzmann factor (BF),

$$\frac{F(|2\rangle)}{F(|1\rangle)} = e^{E_1 - E_2 / kT}$$

(1)

for the ground state |1⟩ and the first excited state |2⟩ in the phonon well. The electron leakage into the continuum depends on the energy of the first electron state which is not bound in the heterostructure design (see Table 1). The occupation at elevated temperatures of this state is also described by eq 1. However, tunneling processes, like the injection and extraction mechanism, suffer from higher barriers due to lower tunneling rates. To compare the effects of different CBOs, we calculate the electron wave functions and energy levels inside the active region for the same layer thicknesses and varying barrier heights using a one-dimensional Schrödinger solver. The change in the energy levels influences the lasing frequency as well as the energy separation in the phonon well, which is crucial for an efficient depopulation of the lower laser state through resonant LO-

Table 1. Band Structure Evaluation for the Structures with Different Al Concentrations at Low Operating Temperatures[a]

	Al% in Al$_x$Ga$_{1-x}$As				
	12%	15%	18%	21%	24%
F_{inj} (kV/cm)	11.44	11.90	12.30	12.65	12.95
F_{ext} (kV/cm)	13.30	13.10	12.86	12.60	12.40
ΔF (kV/cm)	1.86	1.20	0.56	−0.05	−0.55
E_{inj} (meV)	3.76	2.97	2.36	1.88	1.51
E_{ext} (meV)	6.63	5.45	4.50	3.71	3.06
E_{21} (meV)	31.78	34.59	36.9	38.75	40.25
freq (THz)	2.79	2.79	2.75	2.67	2.69
f_{43}	0.77	0.54	0.37	0.245	0.15
BF$_{12}$ (at 200 K)	0.158	0.134	0.118	0.106	0.097
first unbound state (meV)	52	94	103	114	188

[a]F_{inj} and F_{ext} are the bias fields at the minimum energy separation of the injector (E_{inj}) and extraction (E_{ext}) mechanisms. $\Delta F = F_{ext} − F_{inj}$ is the difference of the alignment fields for electron extraction and injection. The energy separation in the phonon well (E_{21}), the lasing frequency, and the oscillator strength f_{43} are given for the average values of F_{inj} and F_{ext}. The Boltzmann factor BF$_{12}$ of the levels |1⟩ and |2⟩ is given for a temperature of 200 K. The energy of the first unbound state is with respect to the upper laser level |4⟩.

phonon depletion. Additionally, the change in the electron wave function affects the oscillator strength (f_{43}) of the optical transition as well as the alignment of the injector and extractor mechanisms for the upper and lower laser state. Figure 3a shows
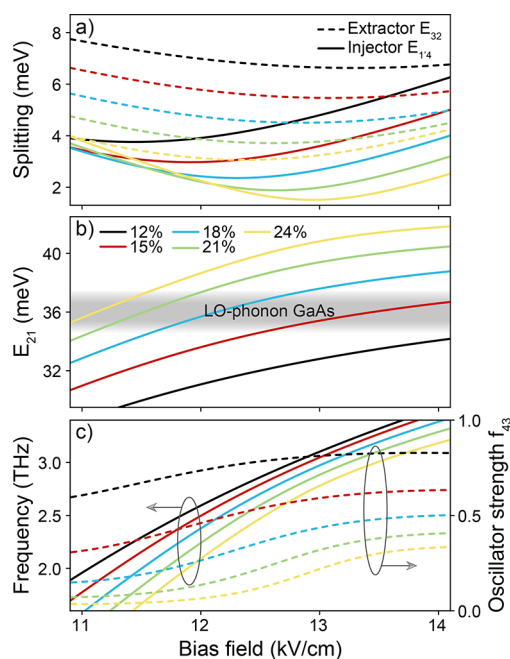
Figure 3. Band structure calculations for different conduction band offsets (CBOs) with Al concentrations of 12−24%. (a) Energy splitting of the injector ($E_{1'4}$) and extractor (E_{32}) indicated in solid and dashed lines, respectively. For low barriers, the injector aligns before the extractor, which changes for higher barriers. (b) The high confinement, due to the higher barriers, increases the energy separation E_{21}, which influences the LO-phonon resonant depopulation mechanism and the thermal backfilling of the lower laser level. (c) Lasing frequency and oscillator strength for the optical transition. A strong influence of the matrix element is depicted leading to a more diagonal transition for higher barriers.

the energy splitting of the injector ($E_{1'4}$) and extractor (E_{32}) as a function of the applied bias field for all five designs. For the lowest barrier structure, the injector is aligning at a bias field 2 kV/cm lower than the extractor. With increasing barrier heights, this difference is reduced. For the Al concentration of 21% the injector and extractor are aligning at the same bias field (see Table 1). For the highest barrier design, the extractor is finally aligning before the injector. One also observes the smaller energy splitting for the higher barriers which changes the tunneling probabilities of the electron injection and extraction mechanisms.

The enlarged electron mode confinement in the wells due to the higher barriers results in an increased separation of the ground state and the first excited state in the phonon well. Figure 3b shows this energy separation E_{21} as a function of the bias field. For the two designs with the lowest barriers this energy separation is below the LO-phonon energy of GaAs (36 meV) while the samples with 21% and 24% Al have a larger energy separation. The LO-phonon assisted relaxation time is dependent on this energy separation[25] and therefore crucial for the depopulation of the lower laser state. When $E_{21} < \hbar\omega_{LO}$, this relaxation can only proceed if the wave vector of the excited state is nonzero, thus the relaxation rate decreases for the low barrier structures. In addition, the energy separation E_{21} changes the thermal backfilling coefficient at high operating temperatures as described in eq 1. At a temperature of 200 K the Boltzmann factor (B_{21}) decreases from 0.158 for 12% Al to 0.097 for 24% Al, hence lowering the thermal backfilling with the higher barriers. Figure 3c depicts the change of the lasing frequency and the oscillator strength (f_{43}) of the lasing transition. For higher barriers, smaller lasing frequencies as well as lower oscillator strengths are predicted from the band structure calculations. The reduction in oscillator strength is due to the more diagonal transition caused by the larger electron confinement of the higher barriers.[26]

These band structure calculations show that larger barrier heights should be beneficial for high temperature operation, as long the modified wave functions do not significantly reduce the electrical stability of the quantum cascade structure or the gain is reduced by the decreased matrix element.

■ EXPERIMENTAL METHOD AND RESULTS

To confirm the above-described hypothesis, we have fabricated the five structures with different barrier heights and measured their optoelectronic behavior. The semiconductor heterostructures of the active regions were grown by molecular beam epitaxy. Each of the five samples consists of 340 periods with a 100 nm thick highly doped contact layer at the top for electron injection, resulting in a total thickness of 15 μm. To reduce parasitic optical losses no contact layer at the bottom was grown. The Al content and layer thickness were determined by high-resolution X-ray diffraction. The deviations from the nominal period thickness ($\Delta D/D$) are listed in Table 2.

From these active regions ridge lasers were processed with a double metal (Au−Au) waveguide geometry[27] and with widths 60−120 μm and lengths 1000−2000 μm. After processing, the samples were indium soldered to a copper plate and mounted on the coldfinger of a helium flow cryostat to perform temperature-dependent light−current−voltage (LIV) measurements. A Fourier-transform infrared (FTIR) spectrometer with an integrated deuterated triglycine sulfate (DTGS) far-infrared detector was used to measure the emitted THz radiation. Figure 4 shows the LIV characteristics for all five different active regions

Table 2. Summary of the Experimental Data for the Five Structures with Varying Al Concentration in the $Al_xGa_{1-x}As$ Barriers[a]

	Al% in $Al_xGa_{1-x}As$				
	12%	15%	18%	21%	24%
$\Delta D/D$ (%)	+0.43	+1.34	+1.23	+1.57	+0.66
J_{th} (A/cm^2)	–	1170	766	536	464
J_{max} (A/cm^2)	–	1900	1116	784	671
$(J_{max} - J_{th})/J_{th}$ (%)	–	62.4	46.8	46.2	44.6
T_{max} (K)	–	163	183	186.5	148
frequency (THz)	–	3.2	2.9	2.7	2.9

[a]$\Delta D/D$ is the deviation of the nominal period thickness (D). The threshold current density J_{th}, the current density at the maximum lasing intensity J_{max}, and the dynamic range is an average over several ridge devices at a temperature of 5 K. The lasing frequency is measured at the maximum intensity at a temperature of 5 K.
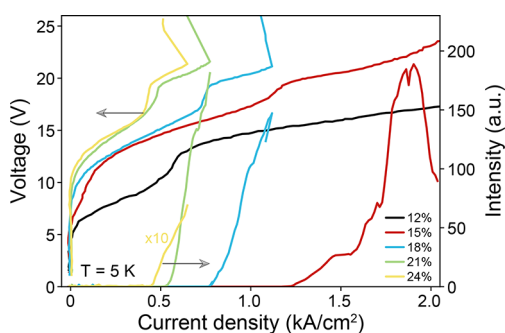
Figure 4. Light−current−voltage measurement in pulsed mode for all five structures at a heat sink temperature of 5 K. The design with 12% Al shows no lasing. The threshold current density decreases for higher barriers. The 15% Al structure shows stable electrical behavior, whereas for higher barriers the structures is electrically instable before the optical output power saturates. The very low oscillator strength of the 24% Al design reduces the output power by more than 1 order of magnitude compared to the other structures. Note that the bias at lasing threshold for all structures is similar.

measured at a heat sink temperature of 5 K. The laser ridges fabricated from the wafer with the lowest Al concentration show comparable high current densities and, as expected, no lasing operation. Their low resistance is a result of the very low barriers and the high electron leakage into continuum. For the samples with higher barriers, we observe decreased threshold current

densities as predicted. Apart from the current density at the lasing threshold, the current density at the maximum intensity decreases as well. For the devices with an Al concentration ≥18%, the maximum intensity occurs at the bias point where the cascade sub-band structure becomes electrically instable, while the 15% Al sample has a normal rollover of the optical output power. This means that for the high barriers samples the gain does not saturate before electrical instabilities occur and the alignment is lost. The current density dynamic range is defined as

$$(J_{max} - J_{th})/J_{th} \tag{2}$$

where J_{th} and J_{max} are the current densities at threshold and maximum intensity. The dynamic range reduces with higher CBOs, indicating that the injector/extractor alignment, which is crucial for a stable electron transport in the heterostructure, exists over a shrinking range. For the sample with the highest CBO, where the extractor mechanism is aligning before the injector, the instability occurs at a low current density and the lasing intensity is more than 1 order of magnitude smaller, compared to other devices.

To investigate the temperature dependence of the electronic transport and the optical gain, LIV data were measured from liquid helium temperatures up to the maximum operating temperature T_{max} of each structure. Figure 5 shows the data for the four samples from which lasing was observed. T_{max} shows an increase up to an Al concentration of 21% with a temperature of 186.5K and then falls considerably for the 24% Al sample. For the sample with 18% Al, the instabilities observed at 5 K in the $I-V$ curve did not appear at elevated temperatures and a rollover of the optical output power can be seen, while for 21% and 24% there is still a breakdown of the electron transport at the maximum operating temperatures. The huge decrease of T_{max} for the 24% Al sample can be attributed to the very high energy splitting in the phonon well and the misalignment of the injector and extractor. The low observed intensity for this structure also proves that the higher barriers reduce the oscillator strength and thus the optical gain.

The spectra at temperatures of 5 K and T_{max} for all four samples are shown in the insets of Figure 5. For the samples from 15% to 21%, a clear decrease of the lasing frequency can be seen, as predicted by the band structure calculations (see Figure 3c). For the 24% sample, the lasing frequency is again higher, which indicates that for this sample the upper lasing level is changed,
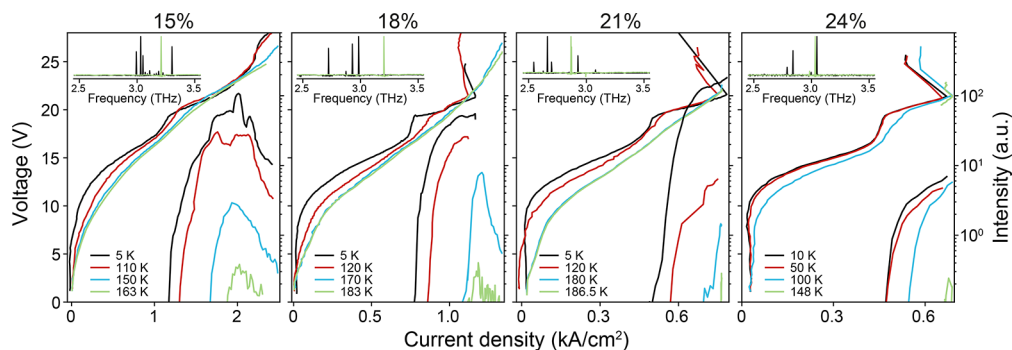

Figure 5. Pulsed LIV measurements for the designs with 15% to 24% Al barriers at different temperatures. At T_{max} the structure with 18% Al shows stable electrical behavior and thus reaches the saturation point of the gain. For the two samples with higher Al content barriers, the electrical instabilities still exist at elevated temperatures; however, the 21% sample shows the highest T_{max} of 186.5 K. The lasing frequencies at 5 K and close to T_{max} are shown in the insets in black and green, respectively.

and the optical transition takes place between the levels $|1'\rangle$ and $|3\rangle$ instead of $|4\rangle$ and $|3\rangle$.

For the 21% sample, the maximum operating temperature of 186.5 K at a lasing frequency of 2.86 THz is a factor of 1.36 significantly above the temperature of $\hbar\omega/k_B$, exceeding the 1.29 value of the temperature record design (199.5 K at 3.22 THz).[7] Although for this structure the energy splitting in the phonon well is larger than the GaAs LO-phonon energy and the electrical properties are not perfect, it shows high temperature operation at this low frequencies with the best reported $k_B T_{max}/\hbar\omega$ value for a three-well active region design. The large energy separation in the phonon well lowers the probability of thermally activated backfilling of the lower laser level and electron leakage into continuum states is suppressed by the higher barriers. The very good performance of this structure is a major breakthrough which proves our hypothesis of high temperature operation for high barrier structures.

■ DESIGN IMPROVEMENT

To further increase the temperature performance and operation range of the 21% Al sample the problems with electrical instability at T_{max} and a low dynamic range, must be solved. A change of the injector/extractor mechanism is necessary to improve the electrical stability of the quantum cascade structure at T_{max}. Additionally, the very high energy separation in the phonon well must be decreased to enhance the LO-phonon depopulation process by tuning the thickness of the phonon well. The increased Al concentration leads to higher barriers and thus to a more diagonal transition. To counteract this lower oscillator strength, the thickness of the radiative barrier is reduced. Considering these requirements, a new structure was designed consisting of three barriers with layer thicknesses **4.3**/9.1/**2.0**/8.7/**3.8**/2/<u>5</u>/9.6 nm starting with the injector barrier, where the AlGaAs barriers are indicated in bold font and the doped region is underlined. Figure 6 shows the calculated
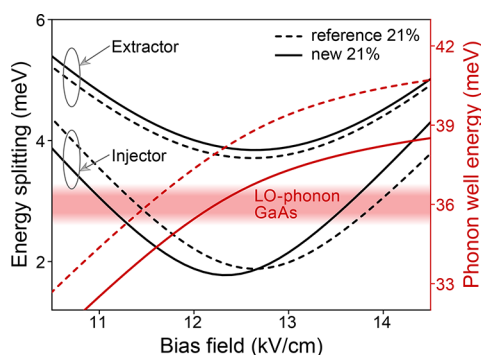
Figure 6. Alignment comparison between the new (solid lines) and reference (dashed lines) structure (both 21% Al in the barriers). For a better electrical stability, the injector of the optimized design is shifted toward a lower bias field. In addition, the energy separation in the phonon well is reduced to match the LO-phonon energy of GaAs.

injector and extractor alignment for the reference and the new structure. As seen from the previous comparison of the calculated alignment bias field of the injector and extractor (Figure 3a) and the measured dynamic range of the five samples with different Al composition (see Figures 4 and 5), we expect an improved electrical stability and thus higher dynamic range if the injector is aligning at a lower bias field than the extractor. Therefore, the injector of the new structure is shifted toward

lower bias fields, whereas the extractor is kept at the same bias field. In addition, the transition energy in the phonon well is lower. The LIV measurement of this optimized structure is shown in Figure 7 (red lines). Due to the slightly thinner barriers
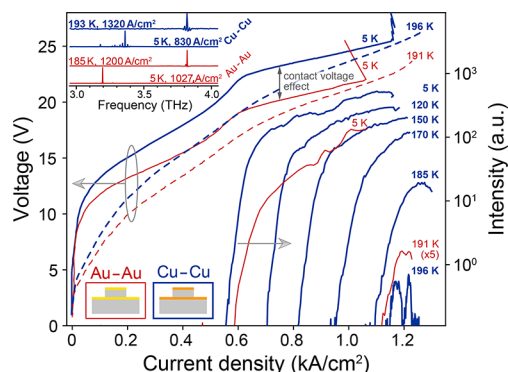
Figure 7. Pulsed LIV measurements of the optimized structure with Au−Au (red lines) and Cu−Cu (blue lines) waveguides. This structure shows electrical stability at T_{max} and an increased dynamic range compared to the reference sample. The structure is lasing up to 191 K with Au waveguides. Changing to Cu claddings lowers the waveguide losses and increases T_{max} to 196 K. The higher bias voltage for Cu waveguides is caused by a higher Schottky voltage drop. Spectra at low and high temperatures close to T_{max} for the Au−Au and Cu−Cu waveguide samples are shown in the inset.

of the structure, the tunneling probabilities are enhanced, leading to higher current densities, compared to the reference sample. In addition, the optimized injector/extractor coupling improves the dynamic range at low temperatures from 46% to 76%. This shows the necessity of the right injector and extractor design to increase the dynamic range of these devices. As discussed in the previous section, a stable electrical behavior at high operating temperatures is essential to reach the maximum gain point of the QCL. The $I−V$ characteristic of this new structure shows stable operating conditions at the maximum operating temperature of 191 K, resulting from the shifted injector mechanism. This operating temperature is the highest reported value for THz QLCs based on Au−Au waveguides. This shows the potential of experimental investigations of THz QCLs in combination with simple one-dimensional band structure calculations to improve the temperature performance of these devices.

To reduce the waveguide losses of the double metal cavity, the same wafer was processed with copper (Cu) waveguide, expected to have lower waveguide losses in this frequency range.[28] The temperature-dependent LIV characterization of these devices is shown in Figure 7 (blue lines). Spectra are depicted in the inset of Figure 7 and show a lasing frequency of 3.4 THz at liquid helium temperature which blue shifts to 3.8 THz at T_{max}, due to different mode selection. The voltage offset compared to the device with Au−Au waveguide results from a higher voltage drop at the Schottky contact. Additionally, the dynamic range at low temperatures is further improved, indicating lower optical losses of the used Cu−Cu waveguides. With this improved copper waveguides operation up to a temperature of 196 K was achieved.

To validate the reproducibility of this design optimization, a second structure with 24% Al barriers was designed. The electron injector and extractor, lasing frequency, oscillator strength and the energy separation in the phonon well are almost

identical to the optimized design with 21% Al barriers. The measured LIV characterization of this adapted 24% Al design shows the same J_{th} and J_{max}. Additionally, Cu−Cu waveguide devices also reach a T_{max} of 196 K.

CONCLUSION

We have studied the influence of different barrier heights for one and the same heterostructure design of a three-well GaAs/AlGaAs THz QCL by changing the Al concentration in the barrier between 12% and 24%. Comparison of results from band structure calculations and measurement data shows how the electron injection and extraction mechanism influences the electrical stability of the lasers. Particularly to achieve high operating temperatures, it is necessary to reach the maximum gain of the laser before electrical instability occurs. The effect of alignment with the resonant LO-phonon is studied, showing higher operating temperatures for an energy separation in the phonon well slightly above the 36 meV LO-phonon energy of GaAs. Furthermore, this higher energy separation reduces the thermal backfilling probability. Higher barriers also reduce electron leakage into the continuum, which is especially important at elevated temperatures due to the occupation of higher electronic states. By analyzing the results of the barrier height study and combining the advantages of the respective structures, we were able to optimize the QCL design in terms of electrical stability. More importantly, the maximum operating temperature was increased to 191 K, which is up to now the highest reported value for a gold waveguide THz QCL.

These results demonstrate remarkably that higher barriers are favored for THz QCLs based on GaAs/AlGaAs, but reduced population inversion at elevated temperature still limits the operating temperature to values below 200 K.

AUTHOR INFORMATION

Corresponding Author
*E-mail: martin.kainz@tuwien.ac.at.
ORCID
Martin Alexander Kainz: 0000-0002-6504-5862
Aaron Maxwell Andrews: 0000-0002-5790-2588
Hermann Detz: 0000-0002-4167-3653
Notes
The authors declare no competing financial interest.

ACKNOWLEDGMENTS

REFERENCES

(1) Köhler, R.; Tredicucci, A.; Beltram, F.; Beere, H. E.; Linfield, E. H.; Davies, A. G.; Ritchie, D. A.; Iotti, R. C.; Rossi, F. Terahertz Semiconductor-Heterostructure Laser. *Nature* **2002**, *417*, 156−159.

(2) Williams, B. S. Terahertz Quantum-Cascade Lasers. *Nat. Photonics* **2007**, *1*, 517−525.

(3) Walther, C.; Fischer, M.; Scalari, G.; Terazzi, R.; Hoyler, N.; Faist, J. Quantum Cascade Lasers Operating from 1.2 to 1.6 THz. *Appl. Phys. Lett.* **2007**, *91*, 131122.

(4) Wienold, M.; Röben, B.; Lü, X.; Rozas, G.; Schrottke, L.; Biermann, K.; Grahn, H. T. Frequency Dependence of the Maximum

Operating Temperature for Quantum-Cascade Lasers up to 5.4 THz. *Appl. Phys. Lett.* **2015**, *107*, 202101.

(5) Tonouchi, M. Cutting-Edge Terahertz Technology. *Nat. Photonics* **2007**, *1*, 97−105.

(6) Richter, H.; Wienold, M.; Schrottke, L.; Biermann, K.; Grahn, H. T.; Hubers, H.-W. 4.7-THz Local Oscillator for the GREAT Heterodyne Spectrometer on SOFIA. *IEEE Trans. Terahertz Sci. Technol.* **2015**, *5*, 539−545.

(7) Fathololoumi, S.; Dupont, E.; Chan, C.; Wasilewski, Z.; Laframboise, S.; Ban, D.; Mátyás, A.; Jirauschek, C.; Hu, Q.; Liu, H. C. Terahertz Quantum Cascade Lasers Operating up to ∼ 200 K with Optimized Oscillator Strength and Improved Injection Tunneling. *Opt. Express* **2012**, *20*, 3866−3876.

(8) Franckié, M.; Bosco, L.; Beck, M.; Bonzon, C.; Mavrona, E.; Scalari, G.; Wacker, A.; Faist, J. Two-Well Quantum Cascade Laser Optimization by Non-Equilibrium Green's Function Modelling. *Appl. Phys. Lett.* **2018**, *112*, 021104.

(9) Adams, R. W.; Vijayraghavan, K.; Wang, Q. J.; Fan, J.; Capasso, F.; Khanna, S. P.; Davies, A. G.; Linfield, E. H.; Belkin, M. A. GaAs/$Al_{0.15}Ga_{0.85}As$ Terahertz Quantum Cascade Lasers with Double-Phonon Resonant Depopulation Operating up to 172 K. *Appl. Phys. Lett.* **2010**, *97*, 131111.

(10) Albo, A.; Flores, Y. V.; Hu, Q.; Reno, J. L. Two-Well Terahertz Quantum Cascade Lasers with Suppressed Carrier Leakage. *Appl. Phys. Lett.* **2017**, *111*, 111107.

(11) Albo, A.; Flores, Y. V. Carrier Leakage Dynamics in Terahertz Quantum Cascade Lasers. *IEEE J. Quantum Electron.* **2017**, *53*, 8500508.

(12) Benveniste, E.; Vasanelli, A.; Delteil, A.; Devenson, J.; Teissier, R.; Baranov, A.; Andrews, A. M.; Strasser, G.; Sagnes, I.; Sirtori, C. Influence of the Material Parameters on Quantum Cascade Devices. *Appl. Phys. Lett.* **2008**, *93*, 131108.

(13) Detz, H.; Andrews, A. M.; Kainz, M. A.; Schönhuber, S.; Zederbauer, T.; MacFarland, D.; Krall, M.; Deutsch, C.; Brandstetter, M.; Klang, P.; Schrenk, W.; Unterrainer, K.; Strasser, G. Evaluation of Material Systems for THz Quantum Cascade Laser Active Regions. *Phys. Status Solidi A* **2018**, 1800504.

(14) Ajili, L.; Scalari, G.; Hoyler, N.; Giovannini, M.; Faist, J. InGaAs−AlInAs/InP Terahertz Quantum Cascade Laser. *Appl. Phys. Lett.* **2005**, *87*, 141107.

(15) Deutsch, C.; et al. High-Power Growth-Robust InGaAs/InAlAs Terahertz Quantum Cascade Lasers. *ACS Photonics* **2017**, *4*, 957−962.

(16) Ohtani, K.; Beck, M.; Scalari, G.; Faist, J. Terahertz Quantum Cascade Lasers Based on Quaternary AlInGaAs Barriers. *Appl. Phys. Lett.* **2013**, *103*, 041103.

(17) Ohtani, K.; Beck, M.; Faist, J. Strain-Compensated InGaAs Terahertz Quantum Cascade Lasers. *ACS Photonics* **2016**, *3*, 2297−2302.

(18) Krall, M. *Nanoscale Transport and Photonic Confinement in Terahertz Quantum Cascade Lasers*; Gesellschaft für Mikroelektronik: Vienna, 2018.

(19) Deutsch, C.; Benz, A.; Detz, H.; Klang, P.; Nobile, M.; Andrews, A. M.; Schrenk, W.; Kubis, T.; Vogl, P.; Strasser, G.; Unterrainer, K. Terahertz Quantum Cascade Lasers Based on Type II InGaAs/GaAsSb/InP. *Appl. Phys. Lett.* **2010**, *97*, 261110.

(20) Brandstetter, M.; Kainz, M. A.; Zederbauer, T.; Krall, M.; Schönhuber, S.; Detz, H.; Schrenk, W.; Andrews, A. M.; Strasser, G.; Unterrainer, K. InAs Based Terahertz Quantum Cascade Lasers. *Appl. Phys. Lett.* **2016**, *108*, 011109.

(21) Lin, T.-T.; Ohtani, K.; Ohno, H. Thermally Activated Longitudinal Optical Phonon Scattering of a 3.8 THz GaAs Quantum Cascade Laser. *Appl. Phys. Express* **2009**, *2*, 022102.

(22) Albo, A.; Hu, Q. Carrier Leakage into the Continuum in Diagonal GaAs/$Al_{0.15}GaAs$ Terahertz Quantum Cascade Lasers. *Appl. Phys. Lett.* **2015**, *107*, 241101.

(23) Deutsch, C.; Detz, H.; Zederbauer, T.; Andrews, A. M.; Klang, P.; Kubis, T.; Klimeck, G.; Schuster, M. E.; Schrenk, W.; Strasser, G.; Unterrainer, K. Probing Scattering Mechanisms with Symmetric Quantum Cascade Lasers. *Opt. Express* **2013**, *21*, 7209.

(24) Deutsch, C.; Detz, H.; Krall, M.; Brandstetter, M.; Zederbauer, T.; Andrews, A. M.; Schrenk, W.; Strasser, G.; Unterrainer, K. Dopant Migration Effects in Terahertz Quantum Cascade Lasers. *Appl. Phys. Lett.* **2013**, *102*, 201102.

(25) Ndebeka-Bandou, C.; Carosella, F.; Bastard, G. *Quantum States and Scattering in Semiconductor Nanostructures*; Advanced Textbooks in Physics; World Scientific: Hackensack, NJ, 2018.

(26) Kumar, S.; Hu, Q.; Reno, J. L. 186 K Operation of Terahertz Quantum-Cascade Lasers Based on a Diagonal Design. *Appl. Phys. Lett.* **2009**, *94*, 131105.

(27) Williams, B. S.; Kumar, S.; Callebaut, H.; Hu, Q.; Reno, J. L. Terahertz Quantum-Cascade Laser at $\Lambda \approx 100 \mu m$ Using Metal Waveguide for Mode Confinement. *Appl. Phys. Lett.* **2003**, *83*, 2124.

(28) Belkin, M. A.; Fan, J. A.; Hormoz, S.; Capasso, F.; Khanna, S. P.; Lachab, M.; Davies, A. G.; Linfield, E. H. Terahertz Quantum Cascade Lasers with Copper Metal-Metal Waveguides Operating up to 178 K. *Opt. Express* **2008**, *16*, 3242.